

Azimuth Variation in Microwave Scatterometer and Radiometer Data Over Antarctica

David G. Long, *Senior Member, IEEE*, and Mark R. Drinkwater, *Member, IEEE*,

Abstract—While designed for ocean observation, scatterometer and radiometer data have proven very useful in a variety of cryosphere studies. Over large regions of Antarctica, ice sheet and bedrock topography and the snow deposition, drift, and erosional environment combine to produce roughness on various scales. Roughness ranges from broad, basin-scale ice-sheet topography at ~ 100 km wavelengths to large, spatially coherent dune fields at ~ 10 km wavelength to erosional features on the meter scale known as sastrugi. These roughness scales influence the microwave backscattering and emission properties of the surface, combining to introduce azimuth-angle dependencies in the satellite observation data. In this paper, we explore the use of NASA scatterometer (NSCAT) data, European remote sensing (ERS) advanced microwave instrument (AMI) scatterometer mode data, and special sensor microwave/imager (SSM/I) data to study surface roughness effects in Antarctica. All three sensors provide strong evidence of azimuth modulation, which is correlated with the surface slope environment and results in a katabatic wind flow regime. Due to its broad azimuth coverage, NSCAT data appears to be the best suited for azimuth-angle observations. A simple empirical model for the azimuth variation in the radar backscatter is developed, and an algorithm for computing the parameters of the model from NSCAT data at a fine scale is presented. Results indicate relationships exist between the azimuthal variation of the data and the orientation of the surface slope and small-scale roughness relative to the sensor-look direction.

Index Terms—Azimuthal anisotropy, backscattering, emissivity, ice sheet, radar, radiometer, sastrugi, scatterometer, surface roughness.

I. INTRODUCTION

WIND scatterometers are designed to measure the normalized radar cross section (σ^o) of the ocean's surface, from which the near-surface wind over the ocean is inferred with the aid of a geophysical model function (GMF) [25]. Scatterometer data are also being exploited in studies of polar ice (e.g., [6], [7], [15], [23], [31], [41], [42]). Microwave radiometers such as the special sensor microwave/imager (SSM/I) [13] have broad application in atmospheric remote sensing over the ocean and provide essential inputs to numerical weather prediction models. SSM/I data has also been used for mapping polar ice (e.g., [38], [43], [44]). Both scatterometers and radiometers provide frequent, global coverage.

Manuscript received May 4, 1999; revised October 18, 1999 and December 12, 1999. This work was supported in part by the Jet Propulsion Laboratory, California Institute of Technology, Pasadena, under contract to the National Aeronautics and Space Administration, Washington, DC.

D. G. Long is with the Electrical and Computer Engineering Department, Brigham Young University, Provo, UT 84602 USA (long@ee.byu.edu).

M. R. Drinkwater is with the Jet Propulsion Laboratory, California Institute of Technology, Pasadena, CA 91125 USA.

Publisher Item Identifier S 0196-2892(00)05680-1.

Over the ocean, the azimuth variations in σ^o in the scatterometer measurements are used to infer the near-surface vector wind (see [25]), which generates the surface waves, causing the azimuth modulation. Over the Antarctic ice sheet, wind-generated roughness and snowlaying combine to produce an anisotropic response. Radiative cooling of surface air masses over the interior ice sheet causes negative buoyancy and the air to sink downslope. The shape of the Antarctic ice sheet imposes a strong topographic control on the drainage of these airmasses as they flow outward toward the coastal margins. Near the coast, winds are funneled by the local terrain into confluence zones, where the strongest wind speeds and persistence are recorded [27]. Antarctic ice sheet surface winds can maintain approximately the same speed and direction for weeks at a time, making them the most persistent winds on Earth [26]. Thus, wind-induced roughness exhibits considerably less temporal variability in direction than ocean winds. As a result, sastrugi and snow drifts form aligned with the wind direction. Their roughness is regionally dependent upon both the shape of the ice sheet directing the flow and variability in the magnitude of the wind vector. Such erosional and depositional features are believed to be the dominant source of the previously observed azimuth variation in σ^o [31]. Because of this persistence in these winds, we assume that the azimuth modulation is stable over a period of several days, thereby permitting us to combine multiple passes in this analysis.

In this paper, we consider data from the NASA scatterometer (NSCAT) [25], flown on the Japanese Advanced Earth Observation Satellite (ADEOS-1), the wind scatterometer mode (hereafter Escat) of the advanced microwave instrument (AMI) flown on the European Remote Sensing (ERS) satellites [1], and SSM/I data to study the microwave response over Antarctica. We examine measurements of σ^o and T_b with respect to the "relative azimuth angle," [i.e., the pointing angle of the antenna relative to north (see Figs. 1 and 2)] reported by the sensor for each measurement. We study the impact the amplitude of the modulation has upon other applications of this data to global change studies and use the directional dependence in the regional modulation, and attempt to map the distribution of aligned surface roughness features. The goal of the present paper is to extend the semi-empirical analysis of [31] to the entire Antarctic ice sheet. We exploit the broad spatial coverage available with NSCAT, incorporating additional information from Escat, and also evaluate the corresponding azimuth variations in SSM/I brightness temperatures. Coupling observations from each of these sensors can shed light on the scattering/emission mechanisms of the firn and permit extraction of key surface and subsurface properties with the aid of inverse modeling. Furthermore, since scatterometer

and radiometer data represent the longest temporal, global microwave datasets, they are increasingly being used as a baseline in global change studies. An understanding of their regional azimuthal tendencies is important, since sampling and analysis procedures may otherwise confuse azimuth modulation with geophysical changes taking place at the ice sheet surface.

After considering relevant background in Section II, the study methodology is described in Section III. Section IV presents key results, and a summary discussion is provided in Section V. Finally, conclusions are presented in Section VI.

II. BACKGROUND

Before describing our research methodology, we provide a brief background, including an overview of previous work and a discussion of the image resolution enhancement method employed. The impact of the azimuth measurement geometry with respect to the ice sheet is also reviewed.

A. Previous Studies

A previous study [31] with Seasat scatterometer (SASS) data has demonstrated clear azimuth dependence in Ku-band σ^o over selected areas of eastern Antarctica, attributed primarily to wind-induced snow drifts, or sastrugi. This same study examined scanning multichannel microwave radiometer data from Nimbus-7 to study surface versus volume scattering. However, azimuth variations in the backscatter were not considered. Previous studies have identified [32], examined [16], [14], and characterized [28] azimuth variations in Antarctic firn using SASS and Escat data. Other investigators [34], [32] also used passive microwave radiometer data in studies of the incidence angle-dependent microwave response. In particular, Rack extended the analysis of scatterometer azimuthal modulations by employing a simple empirical model of the azimuthal variability [28]. More recently, Hyland and Young [14] exploited the same approach with the inclusion of an error term accounting for ambiguities present in fitting relatively poorly characterized azimuthal variability in Escat data. However, neither study attempts to draw the distinction between local slope-induced modulations in backscatter, directionally oriented roughness effects, or the combination of the two. This study extends this work and provides additional characterization of the local incidence-angle influence upon the magnitude of the azimuth modulations, together with a more comprehensive model, which accounts for necessary first and second-order terms due to local slope and azimuth effects, respectively.

B. Resolution Enhancement

The low spatial resolution (25–50 km) of scatterometers and radiometers is suitable for studying large-scale ocean phenomena. However, for some land and ice studies, the low intrinsic resolution can limit the utility of the data. To ameliorate this limitation, resolution enhancement algorithms can be applied. The scatterometer image reconstruction (SIR) algorithm was originally developed for SASS data [24] and has been successfully applied to NSCAT data [20], [30] and Escat data [7], [18]. It has also been adapted for SSM/I data

[19]. Using SIR, multiple passes can be combined to produce enhanced resolution images of the radar backscatter properties and brightness temperatures.

Because scatterometers make measurements over a range of incidence angles, the incidence angle dependence of σ^o must be accounted for. Over a limited incidence angle range of $[20^\circ, 55^\circ]$ σ^o (in dB) is approximately a linear function of θ

$$\sigma^o(\theta) = \mathcal{A} + \mathcal{B}(\theta - 40^\circ) \quad (1)$$

where \mathcal{A} and \mathcal{B} are functions of surface characteristics, azimuth angle, and polarization. \mathcal{A} is the σ^o value at 40° (mid-swath) incidence angle, and \mathcal{B} describes the dependence of σ^o on θ . For scatterometer data, the SIR algorithm produces \mathcal{A} and \mathcal{B} images from multiple passes of σ^o measurements. The \mathcal{A} and \mathcal{B} data provide global images of the mean radar backscatter properties of the surface over the imaging period. The scatterometer-derived backscatter properties can then be related to ice and snow characteristics to study the seasonal evolution of polar ice regions.

Using the SIR with filtering (SIRF) algorithm, dual polarization \mathcal{A} and \mathcal{B} images with an effective resolution of 8–10 km in the polar regions can be generated with six days of NSCAT data. NSCAT V-pol images can be produced with only three days of data or less since there are more V-pol antenna beams than H-pol beams. However, for most studies, six days is used to ensure that the H-pol data provides enough coverage to create reconstructed images. Since the V-pol images are reconstructed with more measurements, the qualities of the V-pol \mathcal{A} and \mathcal{B} images are superior to the corresponding H-pol images. Applied to six days of Escat data in the polar regions, the SIR algorithm produces C-band \mathcal{A} and \mathcal{B} images with an effective resolution of 25–30 km from the nominally 50-km resolution measurements [18]. The resolution improvement for Escat is limited by the spatial resampling filter applied to the Escat data.

Applied to radiometer data, SIR provides enhanced resolution images of brightness temperature based on surface emission modified by the intervening atmosphere. The frequency- and polarization-dependent emission can be related to the geophysical characteristics of the firn and ice characteristics (see for example, [38]). The varying resolution of the SSM/I channels, coupled with their low resolution, can be a limiting factor in the application of the data to snow and ice studies and has led to interest in SSM/I resolution enhancement algorithms [10], [19], [33], [35], [37]. The SSM/I version of the SIR algorithm provides similar enhancement performance to the Backus-Gilbert algorithm with reduced computation [19]. Furthermore, it can be used in combining multiple passes. While SIR can be used with a single pass on radiometer data, to be compatible with the scatterometer data, a six-day time period is used to create the images presented below. Each channel is considered separately. The resulting images represent the average brightness temperature over the imaging period. While seven channels of SSM/I are collected at varying frequency and polarizations, only the 19- and 37-GHz channels are used in this study. SSM/I measurements are made at a nominal incidence angle of 51° .

By applying the resolution enhancement algorithm to the data from each sensor, images of compatible resolution are created

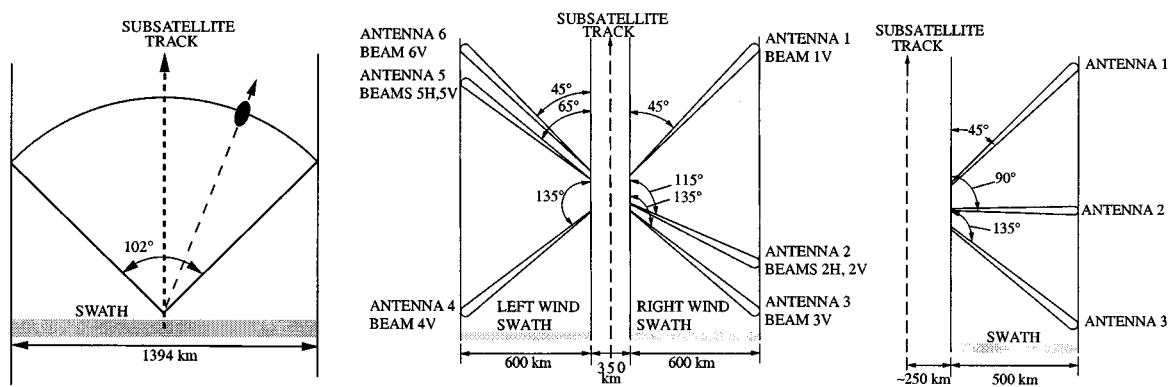


Fig. 1. Illustration of the azimuth measurement geometry for SSM/I, NSCAT, and Escat.

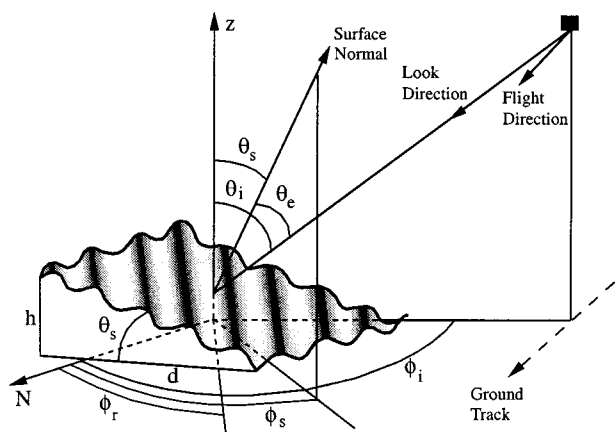


Fig. 2. Figure illustrating the relationship between the azimuth viewing geometry, the local slope, and the incidence angle for a small surface patch. Symbols: θ_i is the incidence angle for a flat surface, θ_s is the local slope, $\theta_e = \theta_i - \theta_s$ is the effective incidence angle, ϕ_i is the azimuth look direction, ϕ_s is the local slope direction, and ϕ_r is the angle of the azimuth roughness, all relative to north.

on an identical grid. This simplifies comparisons between sensors. Image samples for each image type from each sensor are shown in Fig. 3.

C. Azimuth Observation Geometry

The characteristics of each sensor provide unique opportunities and challenges to an azimuth-angle study of Antarctica. For example, with its right-looking, single-sided swath, the Escat orbit, optimized for ocean observation, limits the southernmost extent of Escat data to 79.5° S, while the NSCAT data covers Antarctica to within 1.2° of the pole with its dual-sided swath, and the SSM/I swath data provides comparable coverage to within 2° of the pole. In Fig. 2, we define the azimuth angle as the angle measured clockwise from the meridian, passing through the surface observation to a horizontally-projected line drawn along the boresight of the instantaneous field of view during cell measurement. This definition applies equally to the scatterometer or radiometer observations. Fig. 2 also defines azimuth angles, which indicates the orientation of the local slope normal and the azimuthal orientation of sastrugi. For later discussion, the azimuth direction (the azimuth angle of the

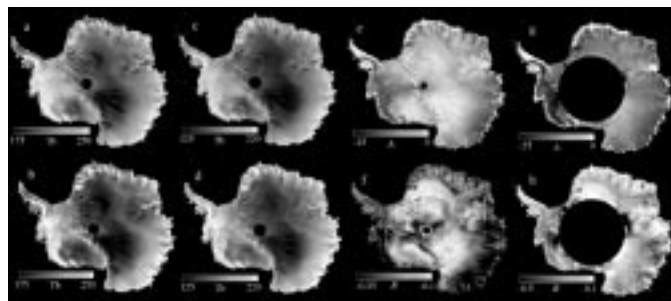


Fig. 3. SSM/I-, NSCAT-, and Escat-derived images of Antarctica produced with the aid of the SIR algorithm from six days of data (JD 277-282). (a) T_b at 19 GHz V-pol, (b) T_b at 19 GHz H-pol, (c) T_b at 37 GHz V-pol, (d) T_b at 37 GHz H-pol, (e) \mathcal{A} at 14 GHz V-pol, (f) \mathcal{B} at 14 GHz V-pol, (g) \mathcal{A} at 5.3 GHz V-pol, and (h) \mathcal{B} at 5.3 GHz V-pol. NSCAT 14 GHz H-pol \mathcal{A} , and \mathcal{B} images are not shown. The NSCAT 4.45-km pixel resolution has been averaged down to 8.9-km resolution to match the SSM/I and Escat image pixel resolution.

projection of the surface normal onto a plane locally tangent to the geoid) is denoted ϕ_s . The azimuth orientation of surface corrugations such as sastrugi is denoted ϕ_r .

Fig. 1 illustrates the relative azimuth geometries of each of the sensors used in this study. NSCAT and Escat use both forward- and aftlooking antennas to make observations of the same point within the measurement swath at multiple azimuth angles. However, since the SSM/I is a forwardlooking-only instrument, it is capable of only a limited range of azimuth angle observations of a given point on the earth. For all the sensors, over a multiple-day period, depending on the location and details of the orbit geometry, a given area is observed several times at different geometries due to the shift in the ground track of the orbit with time. While SSM/I measurements are made at only a single incidence angle, the scatterometer measurements span a range of incidence angles. Hence, as noted previously, the variation in the backscatter with incidence angle must be accounted for.

For a given point on the Earth’s surface, the antenna azimuth geometries of NSCAT and Escat generally result in a discrete set of azimuth angle observations. This is because multiple antennas at various azimuth angles are used to make the measurements. Each discrete azimuth sampling is thus the result of measurements from a distinct beam on a specific reference orbit. Typically, each beam observes the study area once on an ascending (northbound) orbit pass and again on a descending (southbound) orbit pass over the area, resulting in two different

relative azimuth angles due to the angle of the orbit pass with respect to the ground. For NSCAT, there are six V-pol antenna azimuth angles (three on each side), resulting in 12 different V-pol azimuth observations, but only a single H-pol beam per side, resulting in four different H-pol azimuth observations. Escat has only three beams on a single side of the spacecraft and thus a maximum of six discrete azimuth angles measured on both ascending and descending passes. In practice, the symmetric geometry of the Escat antennas, coupled with the orbit geometry with respect to the Antarctic ice sheet, reduces the number of unique azimuth angle observations to somewhat less than this. For all sensors, the range of azimuth angles varies with Antarctic location due to the combination of orbit and swath geometries.

III. ANALYSIS METHODOLOGY

The goal of this paper is to examine the azimuth dependence of the microwave signature of Antarctica using data from NSCAT, Escat, and SSM/I. Coupling all of these observations can shed light on the scattering/emission mechanisms of the firm and permit extraction of key surface and subsurface properties with the aid of inverse modeling.

The general approach employed in this study is to generate images of scatterometer \mathcal{A} and \mathcal{B} and radiometer T_b and, with the aid of these images, select a limited set of study regions to evaluate the azimuth modulation of the measured parameters. We then develop an empirical model for the azimuth modulation and a method to estimate parameters of the model from NSCAT data at enhanced resolution. Resulting fitted parameters are evaluated with relationship to the local topography and known katabatic wind flow patterns.

A. Sensor Images

To provide an initial Antarctic-wide view of each sensor's observations, the appropriate version of the SIR algorithm is applied to data collected by each sensor over the six-day study period to generate images on the same projection and at the same pixel spacing. The effective resolutions of the images vary, however, between sensors. The imaging period was selected during the 1996 Austral winter (JD 277-282) to minimize seasonal and diurnal impact of air-temperature forced variations in the microwave signatures. The resulting comparison images are shown in Fig. 3.

Upon examining these images, a number of observations can be made. For example, we note the significant differences between the brightness temperature responses at V and H-pol, with V-pol temperatures consistently higher by around 40–50 K at 19 GHz and 25–30 K at 37 GHz. Another striking feature of the images is the distinctive inverse relationship between the T_b and \mathcal{A} values. The T_b images have their lowest brightness temperature values where the \mathcal{A} image has the largest backscatter values. This inverse correlation in the mean brightness temperatures and frequency-dependent backscatter coefficient is treated in more detail in [3] and is not considered further here.

B. Study Regions

Based on subjective examination of the images in Fig. 3, a total of eleven study regions over Antarctica were selected (see

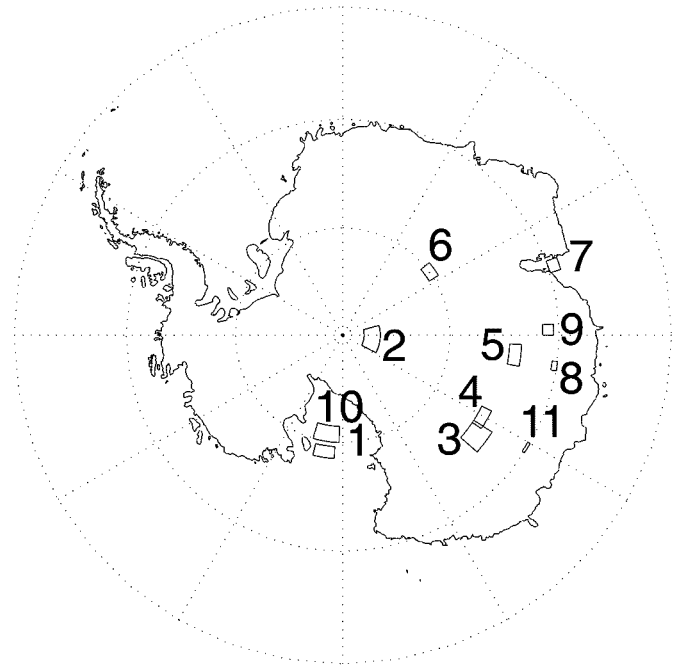


Fig. 4. Map of the locations of key study areas.

TABLE I
STUDY AREAS (DEFINED BY A
RECTANGULAR AREA IN LONGITUDE AND LATITUDE) AND CORRESPONDING
MEAN SURFACE ALTITUDE (IN M), SLOPE (IN M/KM), AND DIRECTION
 ϕ_s (IN DEGREES RELATIVE TO NORTH) DERIVED FROM THE DIGITAL
ELEVATION MAP (DEM) DESCRIBED IN THE TEXT

Area Number	Lower-Left Corner		Upper-Right Corner		Mean DEM		
	lon	lat	lon	lat	Altitude	Slope	Direction
1	-166	-78.5	-176	-79.6	54	0.14	192
2	118	-86.5	75	-88	3106	1.50	179
3	131	-75.5	123	-73.5	3186	0.95	219
4	124	-75.5	117	-74.5	3210	0.73	189
5	100	-73.4	93	-74.5	3509	1.34	233
6	58	-80.5	50	-79.5	3697	1.22	119
7	73.25	-69	70	-70	52	0.65	179
8	97	-70.5	99.5	-70	2661	3.16	218
9	90	-71.5	87	-70.5	2826	3.00	158
10	-164	-81.5	-178	-80	51	0.45	181
11	123	-70.25	120	-70	2451	3.45	225

Fig. 4) to span a variety of surface characteristics. The study areas are listed in Table I together with their extent in longitude and latitude. The locations and extents of the various study areas were chosen to span a variety of surface conditions, while still exhibiting a generally spatially homogeneous response, as observed in the images in Fig. 3. For convenience, the example study areas are selected primarily within East Antarctica (the lower-right quadrant of the images).

Study areas 1, 7, and 10, which are located on the Ross and Amery ice shelf regions (see Fig. 4), exhibit high mean backscatter values but also the least azimuthal anisotropy. Though this in itself is a significant finding, these samples are not considered any further in this paper. For illustration purposes only, the following subsample of study areas shown in Fig. 4 are selected for presentation. Study area 2 is close to the South Pole (at mean 3106 m elevation, see Table I) and area 5 (73.45° S, 100° E) is in Queen Mary Land at a mean elevation of 3509 m (near the old Komsomolskaya Russian

station). Study area 8 (70.55° S, 90° E) lies further downslope at 2661 m (near the old Pionerskaya Russian station), while areas 9 (71.55° S, 90° E) and 11 (70.25° S, 123° E) lie to the west and east in Wilhelm II Land (at 2826 m) and Wilkes Land (at 2451 m), respectively. Area 9 was chosen in particular to facilitate a comparison between the results of this study and those of [28], while area 11 has the largest mean slope of all samples at $\sim 0.2^\circ$ (3.45 m/km).

IV. RESULTS

Beginning with a simple examination of the variations in σ° and T_b with relative azimuth angle for each study area, we develop a simple empirical model to describe the variation of these parameters with relative azimuth and, in the case of the scatterometer data, incidence angle. A method for extracting the parameters of the model from the measurements at the (enhanced) resolution of the images is then presented and the results discussed.

A. Azimuth Angle Modulation

As an initial evaluation of the variation in σ° and T_b with azimuth angle, SSM/I, NSCAT, and Escat data over the sixteen day period between JD 268 and 283, 1996, were accumulated for each of the study areas. Of the eleven study areas, five of them (areas 2, 5, 8, 9, and 11) exhibit significant azimuth modulation in the SSM/I data. The analysis, therefore, focuses on these areas. Scatterplots of T_b versus the relative azimuth angle (SSM/I) and σ° versus relative relative azimuth angle (NSCAT and Escat) are shown later. Since σ° is a strong function of incidence angle [see (1)], the scatterometer data is divided into incidence angle bins, with separate plots generated for each incidence bin. Bins are centered at 20° , 30° , 40° , and 50° . Only scatterometer measurements with incidence angles within $\pm 3^\circ$ of the bin center are used in a given bin, thus minimizing the incidence angle variation of the data.

Scatterplots of T_b and σ° versus azimuth angle are shown in Figs. 5–7. In these plots, measured values are shown as grey points. These individual measurements are binned into $\pm 3^\circ$ azimuth angle bins with the mean and the standard deviation indicated with a dark point with one sigma error bar.

Study area 2 (Fig. 5) exhibits the most noticeable SSM/I azimuth modulation of all the study regions, as well as the widest range of measurement azimuth angles in the SSM/I data due to its proximity to the pole. Although the NSCAT measurements span a wider azimuth angle range than the SSM/I measurements, azimuthal modulations are observed in both datasets. An NSCAT incidence angle of 50° was chosen to most closely match the SSM/I data. Clear azimuthal variation is apparent in the mean brightness temperatures of all channels, with a peak at 220° and troughs at 135° and 315° . Both the mean T_b and the modulation depth (peak-to-trough difference) of T_b versus azimuth angle vary between channels. The comparative scatterplot of the incidence angle NSCAT data (Escat coverage does not extend over study area 2, so no measurements are available from this sensor) shows a weak variation of σ° versus azimuth angle, with the mean σ° higher for V-pol than for H-pol by ~ 1.5 dB.

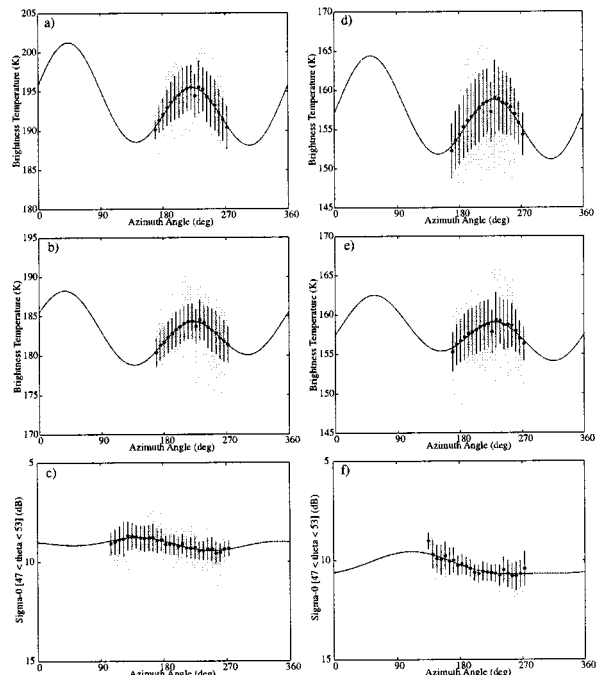


Fig. 5. Scatterplots of T_b and σ° versus azimuth angle for study area 2. (a) SSM/I 19v, (b) SSM/I 19h, (c) SSM/I 37v, (d) SSM/I 37h and NSCAT, (e) V-pol, and (f) H-pol at 50° incidence angle. In this and later figures, values are shown as gray dots, the means of $\pm 3^\circ$ -wide bins are shown as asterisks. The solid vertical lines indicate plus and minus one standard deviation about the mean. Scatterometer statistics are computed in dB. The solid lines represent the second-order azimuth fit (see text).

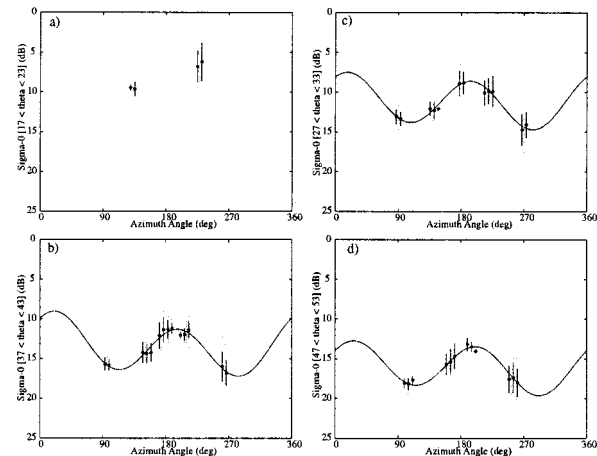


Fig. 6. Escat σ° measurements at various incidence angles from area 5. Measurements are from $\pm 3^\circ$ of the central incidence angle. Left to right, top to bottom, the central incidence angles are 20° , 30° , 40° , and 50° . The solid lines represent the second-order azimuth fit (see text).

We note that the vertical spread in the data at a particular azimuth angle in Fig. 5 is primarily due to noise, with a contribution due to spatial inhomogeneity over the study region. Careful examination of data reveals that there is little apparent correlation between location and parameter value within a given study region. In both NSCAT and SSM/I, the vertical spread in the data is significant compared to the variations in the mean parameter value versus azimuth angle. Peak-to-trough amplitude variation in the binned mean is approximately 5 K and 0.8 dB, while the standard deviations are approximately 3–4 K and 0.5 dB for

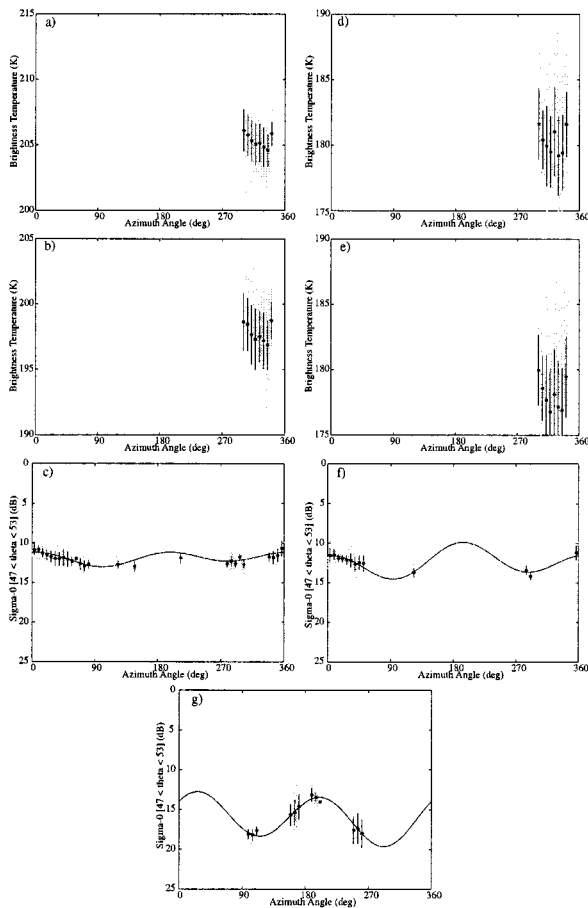


Fig. 7. Scatterplots of T_b and σ^o versus azimuth angle for study area 5. (a) SSM/I 19v, (b) SSM/I 19h, (c) SSM/I 37v, (d) SSM/I 37h, NSCAT, (e) V-pol, (f) H-pol at 50° incidence angle, and (g) Escat V-pol at 50° incidence angle. The solid lines represent the second-order azimuth fit (see text).

SSM/I and NSCAT data, respectively. We note that for the range of azimuth angle available, T_b peaks at approximately 220° , while σ^o peaks at approximately 160° . As previously noted, this type of anticorrelation of active and passive signatures has been previously observed and is explained in more detail in [3].

A similar plot for study area 5 is shown in Fig. 7. We note that the SSM/I data exhibit a smaller azimuth angle range than for study area 2. NSCAT data exhibit measurements at a number of essentially discrete azimuth angles, spread over the full 360° range. Both of these behaviors are typical of all the study areas, region 2 being an exception. SSM/I data suggest a variation in T_b with azimuth angle, but the limited azimuth angle range of the measurements makes conclusions about the azimuth behavior of T_b speculative. On the other hand, the NSCAT measurements span the full 360° range and clearly show modulation [2–3 dB, depending on the polarization; see Fig. 7(c), (f)] in the observed Ku-band σ^o as a function of the azimuth angle. The more limited azimuth angle observations of the Escat data [Fig. 7(g)] suggest a greater modulation at C-band. Only from the NSCAT V-pol data can a peak in the azimuth modulation (at approximately 5°) be determined with confidence.

Comparing the general behavior of σ^o versus azimuth angle and T_b versus azimuth angle in Figs. 5 and 7, we note a difference in the modulation phase (i.e., a decrease in T_b with azimuth

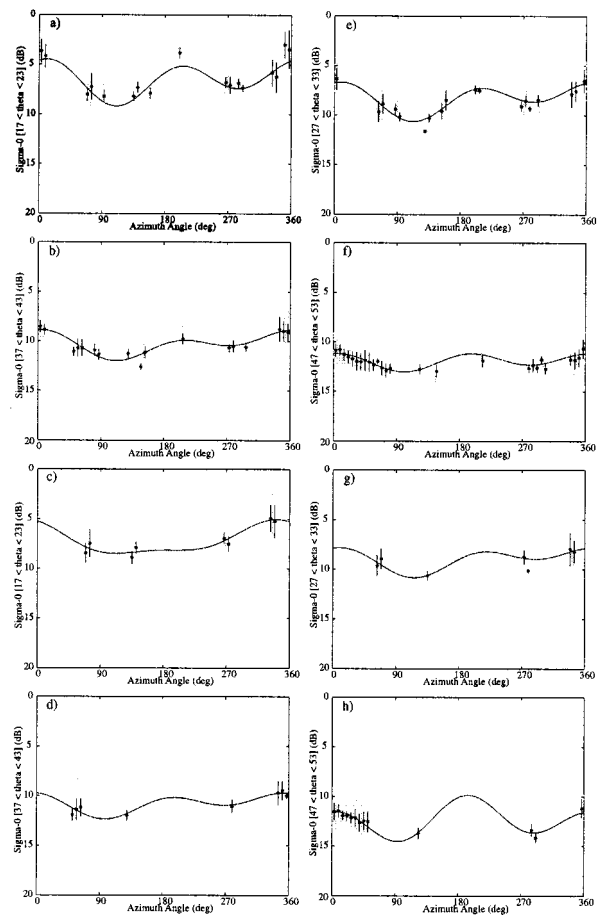


Fig. 8. NSCAT σ^o versus azimuth angle at various incidence angles for study area 5: V-pol (top four plots), H-pol (bottom four plots). Measurements are from $\pm 3^\circ$ of the central incidence angles of 20° , 30° , 40° , and 50° . The solid lines represent the second-order azimuth fit (see text).

angle is accompanied by an increase in σ^o). At present, the precise scattering mechanism remains unvalidated, but on the basis of the observed anticorrelation between σ^o and T_b [3], the regional surface conditions responsible for anisotropic backscattering also appear to result in modulations in the emissivity and therefore, the effective brightness temperature of the surface. Though the modulation depths and locations of the modulation minima vary with the study area, examination of the results from all the study areas yield similar conclusions. As will be shown later, the locations of the maxima and minima are highly correlated with the direction of the katabatic wind.

B. Incidence Angle Dependence

Noting the dependence of σ^o on incidence angle, we investigate the dependence of the azimuth modulation on incidence angle in NSCAT and Escat data. Though not without limitations, the NSCAT data is best-suited for this investigation since it spans a wide range of incidence and azimuth angles: SSM/I observations are limited to a single incidence angle and Escat has limited azimuth sampling.

Fig. 8 shows scatter plots of NSCAT σ^o versus azimuth angles for both V and H-pol observations at incidence angles of 20° to 50° for study region 5. Fig. 6 provides a similar plot for Escat

TABLE II
FOURIER SERIES FIT COEFFICIENTS FOR NSCAT DATA AT VARIOUS INCIDENCE ANGLES FOR STUDY AREA 5. IN THIS TABLE, $M_i = \sqrt{I_i^2 + Q_i^2}$,
 $\phi_i = \tan^{-1} Q_i/I_i$ ANGLES ARE IN DEGREES

Incidence Angle	V Pol									
	I_0	I_1	Q_1	M_1	ϕ_1	I_2	Q_2	M_2	ϕ_2	ψ_0
20°	-6.6	0.605	-0.734	0.951	-50.6	1.375	1.006	1.704	36.2	111
30°	-8.3	0.617	-0.841	1.043	-53.7	0.997	0.795	1.275	38.5	112
40°	-10.3	0.720	-0.624	0.953	-40.9	0.738	0.407	0.843	28.9	112
50°	-11.9	0.068	-0.351	0.358	-79.1	0.686	0.263	0.734	21.1	100
H Pol										
20°	-7.2	1.449	-0.634	1.581	-23.6	0.504	-0.294	0.584	30.3	112
30°	-9.0	0.548	-0.786	0.958	-55.1	0.599	0.636	0.873	46.7	116
40°	-10.8	0.281	-0.679	0.735	-67.5	0.804	0.099	0.810	7.0	97
50°	-12.4	-0.755	-0.591	0.959	141.9	1.545	0.571	1.647	20.0	93

data. These plots are typical of all the study regions where relatively strong azimuth modulation is observed. In addition to the clear variation in the mean σ° with incidence angle, examination of these plots suggests that the modulation depth varies inversely with incidence angle, at least for V-pol. For example, the modulation depth for NSCAT V-pol varies from 5 dB at 20° incidence down to 2 dB at 50° incidence. Also, there appears to be negligible variation in the locations of the minima and maxima of the modulation as a function of incidence angle. The reduced spread in the azimuth observations for H-pol NSCAT makes interpretation of the data more difficult, but it is assumed that the general H-pol azimuth modulation characteristics are similar to V-pol. A similar azimuth sampling limitation occurs for Escat data, making it impossible to characterize the modulation in the 80° to 280° azimuth range. Furthermore, the vertical spread in the Escat data at a given azimuth angle is significant compared to the modulation depth, which masks any variation with incidence angle. The increased penetration of the C-band data may account for the greater variance in the data and the lack of a clear relationship with incidence angle.

A second-order ($N = 2$) Fourier series (in azimuth angle, ϕ_i) of the form

$$\sigma^\circ(\text{dB}) = I_0 + \sum_{k=1}^N [I_k \cos k\phi_i + Q_k \sin k\phi_i] \quad (2)$$

is individually fit (in the least-squares sense) to each of the σ° versus azimuth angle scatterplots in these figures and plotted as a solid curve. The resulting coefficients for NSCAT data are tabulated in Table II for the study region 5 data shown in Fig. 8. The obvious asymmetric nature of the σ° modulation with azimuth angle suggests that both the first and second-order terms in (2) are required to fit the data. We note that due to the reduced number of azimuth observations, the coefficients of the second-order terms in (2) are significantly reduced for H-pol versus V-pol at low incidence angles with a reversal at high incidence angles. As before, there are fewer azimuth observations for Escat than for NSCAT V-pol, although the Escat data in Fig. 6 clearly indicate asymmetry in the modulation.

Simulations suggest that the accuracy of the Fourier series coefficients is affected by the azimuth sampling, with larger errors when the observations do not span the full 360° range. In particular, inadequate sampling affects the location of the azimuth modulation minimum, denoted by ψ_0 . Simulations suggest that

the azimuth sampling of both NSCAT H-pol and Escat measurements is inadequate for accurately estimating both azimuth modulation terms simultaneously over all areas. As a result, the primary analysis in the remainder of the paper is done using NSCAT V-pol observations, with limited comparisons to Escat data. The azimuth sampling deficiency of Escat data is seen as a key limitation in previous studies [14], [28] of the azimuth modulation. Both previous studies assumed a simple periodic function characterized by a single term $\cos(2\phi_i - \text{constant})$, and this prevents characterization of the asymmetry of the modulation pattern.

C. Azimuth Modulation Modeling

It is clear from the analysis presented in the previous section that both first and second harmonic terms are required to describe the azimuth dependence of σ° at a given incidence angle. To account for the variation in both incidence angle and azimuth angle, a simple empirical model is developed. Borrowing from ocean scattering theory, a simple second-order harmonic model is assumed for the variation in σ° (in dB) with azimuth and incidence angles

$$\begin{aligned} \sigma^\circ(\theta, \phi_i) = & \mathcal{A} + \mathcal{B}(\theta - 40^\circ) + M_1 \cos(\phi_i + \phi_1) \\ & + M_2 \cos(2\phi_i + \phi_2) \end{aligned} \quad (3)$$

where \mathcal{A} and \mathcal{B} are defined as before, M_1 and M_2 are the magnitudes of the first-order and second-order azimuth angle harmonic terms, respectively, ϕ_1 and ϕ_2 are the phase angles of the first-order and second-order azimuth angle harmonic terms, respectively, and ϕ_i is the observation azimuth angle relative to north (see Fig. 2).

As suggested by the plots in Fig. 8 and in similar plots for the other study areas, M_1 and M_2 vary with incidence angle. Noting that the dependence of the azimuth modulation depth in dB is often nearly linear with incidence angle, a very simple model is adopted for the dependence of M_1 and M_2 on incidence angle

$$M_1 = c_1 + d_1(\theta - 40^\circ) \quad (4)$$

$$M_2 = c_2 + d_2(\theta - 40^\circ). \quad (5)$$

Normalizing the incidence angle to 40° in (3)–(5) is done primarily for convenience.

The simple model for $\sigma^\circ(\theta, \phi_i)$ described by (3)–(5) will be termed “I model” hereafter. Least-squares estimation is used to simultaneously estimate the I model parameters from the

TABLE III
COEFFICIENTS OF THE AZIMUTH MODULATION MODELS FOR 4 POL NSCAT
DATA IN STUDY AREA 5

Coefficient	I Model	F Model
\mathcal{A}	-10.3	-10.1
\mathcal{B}	-0.198	-0.212
c_1	0.713	0.702
d_1	-0.014	—
ϕ_1	-46.6	-49.0
c_2	1.018	0.950
d_2	0.045	—
ϕ_2	35.1	31.3
ψ_0	107	112

NSCAT V-pol measurements. The values of the I model parameters (\mathcal{A} , \mathcal{B} , c_1 , d_1 , ϕ_1 , c_2 , d_2 , and ϕ_2) for study area 5 are tabulated in Table III. The azimuth angle corresponding to the minimum azimuth modulation is denoted by ψ_0 and is also listed in this table.

Unfortunately, as previously noted, the azimuth/incidence angle sampling varies with location. This can lead to an ill-conditioned least-squares estimation problem in some locations. Under such circumstances, reasonable estimates of the model parameters can often be obtained by separately estimating \mathcal{A} and \mathcal{B} , ignoring the azimuth angle dependence. Then, the σ° measurements are “corrected” by the estimated \mathcal{A} and \mathcal{B} values. Ignoring \mathcal{B} , the remaining model parameters are estimated by ignoring the incidence angle variation in M_1 and M_2 (i.e., setting d_1 and d_2 to zero). This model formulation will be termed the “F model.” The coefficients of the various model formulations are compared in Table III. We note that while the F model is suboptimal compared to the I model formulations as discussed below, it is useful in evaluating key characteristics of the azimuth modulation.

To visualize the behavior of $\sigma^\circ(\theta, \phi_i)$ at Ku-band V-pol, a plot of the I model predicted $\sigma^\circ(\theta, \phi_i)$ is shown in Fig. 9 for study areas 5, 8, 9, and 11. We note a generally similar behavior in all of the study regions with ridge peaks and troughs. At a given incidence angle, σ° exhibits a peak at 5° to 25° and a minimum (ψ_0) at 100° to 120° , depending on the area. Area 5 exhibits the smallest incidence angle dependence.

Over the ocean, a plot of $\sigma^\circ(\theta, \phi_i)$ where ϕ_i is the direction of the radar illumination exhibits the same general behavior as the plots in Fig. 9. For ocean wind applications, $\sigma^\circ(\theta, \phi_i)$ is wind speed dependent and is known as the GMF (see for example, [25]). A similar behavior is observed in radiometer data [40]. Over the ocean, the highest ridge peak in $\sigma^\circ(\theta, \phi_i)$ corresponds to the upwind direction, the other peak corresponds to the downwind direction, and the troughs correspond to the crosswind direction. Since on the ice sheets the sastrugi are aligned approximately in the wind direction (rather than orthogonal-like ocean waves), troughs in the surface roughness are aligned in the upwind and downwind directions and the peaks to the crosswind direction. For ice, the minimum of the backscatter versus azimuth direction generally corresponds to the wind direction (i.e., ψ_0 and ϕ_r generally correspond), with some modification due to incidence angle effects. Since the local topographic slope and km-scale snow dunes modify the local incidence angle, the asymmetry in the modulated backscatter

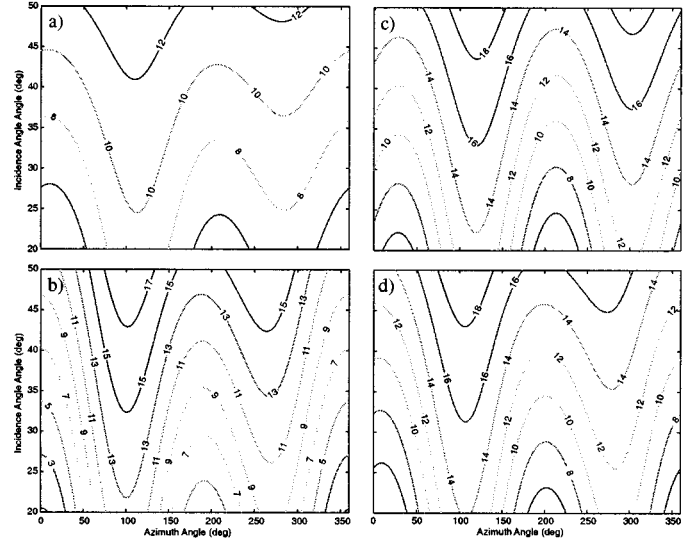


Fig. 9. Contour plots of $\sigma^\circ(\theta, \phi_i)$ computed from the azimuth modulation model parameters estimated from V-pol NSCAT data for study areas (a) 5, (b) 9, (c) 8, and (d) 11. For these areas, ψ_0 is just to the right of the 100° azimuth angle.

results from looking in the upslope and downslope direction. Thus, it is possible to unambiguously infer the wind direction from the σ° measurements.

We note that over the ocean, $\sigma^\circ(\theta, \phi_i)$ is independent of location if ϕ_i is replaced by the relative azimuth angle between the radar illumination angle and the wind direction. Given two or more azimuth observations of σ° , it is then possible to retrieve the near-surface wind vector (e.g., [25]). Unfortunately, the Antarctic surface has variable composition, with spatial variations in firn density, layering, and other effects. Thus, $\sigma^\circ(\theta, \phi_i)$ can be expected to be different at different locations, making an ocean-like wind vector (both speed and direction) retrieval scheme difficult. Nevertheless, it is possible to infer the average wind direction at a given point on the surface if the azimuth sampling is adequate enough to correctly identify the location of the maximum or minimum value in the σ° versus azimuth angle curve.

A careful examination of the observed variation in σ° at a given incidence angle for all the study regions shows that the peaks in the azimuth modulation tend to be somewhat more peaked than predicted by the second-order Fourier series. This phenomena has been observed in ocean scattering, where the peaks in the modulation are somewhat narrower than the troughs [17]. While the inclusion of additional terms in the Fourier series can reduce the residual fit error, they offer only limited insight into the wind direction estimation problem. They are also less tenable due to the limited azimuth sampling.

D. Azimuth Modulation Observation

In order to evaluate the dependence of σ° on the wind direction, a detailed knowledge of the incidence angle variation of M_1 and M_2 is not required. Instead, for wind direction estimation, the primary interest is in the location of the upwind, upslope peak in the azimuth modulation. Knowledge of the depth of the modulation is not required. This enables use of the F model rather than the full I model. Given the parameters of

either model, the angle ψ_0 corresponding to the azimuth angle of the minimum value of σ° can be computed from M_1 and M_2 . We note that the value of ψ_0 estimated from the F model is within approximately 5° of that computed from the full I model (see Table III). Thus, we infer an approximate directional precision of $\pm 5^\circ$ in retrieved direction of the maximum azimuth modulation for NSCAT V-pol.

Using NSCAT data, the azimuth modulation can be evaluated over virtually the entire Antarctic continent. To aid in this evaluation, the following algorithm for evaluating azimuth variation (or modulation) at each pixel in the SIR imagery is used. To compute the model parameters, the SIRF algorithm is first used to compute \mathcal{A} and \mathcal{B} images from the σ° measurements [24]. A polar stereographic projection is used (see Fig. 3) with a nominal pixel resolution of 4.45 km. The effective resolution is approximately 8–10 km. Then, for each σ° measurement, the forward projection [24] is computed from the images. The projection error is the difference between the forward projection and the measurement. Ideally, the projection error is zero, but azimuth modulation and noise result in nonzero projection errors. Any temporal variation of the surface backscatter response over the data collection interval also contributes to a nonzero forward projection. The F model parameters c_1 , c_2 , ϕ_1 , and ϕ_2 (and a residual constant term added to \mathcal{A}) are estimated for each pixel in the enhanced resolution image from the projection errors. For each pixel, the projection errors of each of the σ° measurements that cover the pixel are accumulated and used to estimate the model parameters via least-squares. To reduce the noise level in the NSCAT estimates, a 3×3 edge-preserving median filter is applied to the sine and cosine component images prior to estimation of the magnitude and phase images. From the values of c_1 , c_2 , ϕ_1 , and ϕ_2 , ψ_0 is computed. It should be noted that NSCAT measurements do not cover the area directly around the South Pole and have reduced accuracy in estimating \mathcal{B} near the southernmost coverage limits. A similar algorithm is applied to Escat data using SIR-produced images, though the median filtering step is not applied. However, the limited azimuth sampling of Escat results in less accurate model parameter estimates.

A metric for evaluation of the accuracy of the model is the variance (or, equivalently, the standard deviation) of the residual projection error when the azimuth modulation is disregarded or alternatively taken into account. An NSCAT image of the standard deviation of the projection error for each pixel when the azimuth modulation is not taken into account is shown in Fig. 10(a). This error results from using only the \mathcal{A} and \mathcal{B} coefficients and has a standard deviation which varies from 0 to 2.5 dB. The largest values tend to occur in East Antarctica, where strong azimuthal modulations occur as a result of directional anisotropy in the backscatter. Error standard deviations exceeding 2 dB are noted in George V Land, over large parts of Wilkes Land, and in Princess Elizabeth Land and Wilhelm II Land. The residual error after taking azimuth modulation into account is the difference between the observations and the forward projection plus the predicted azimuth modulation. Fig. 10(b) shows the standard deviation of this residual error, which is significantly reduced compared to the projection error. Visible in both the projection and residual standard deviation images are regional features associated with the azimuth modulation (and discussed

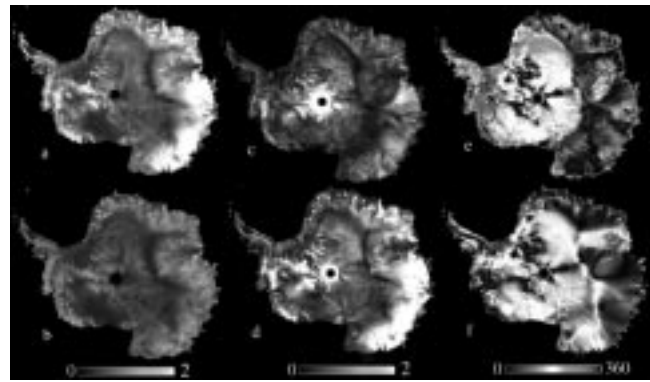


Fig. 10. NSCAT images from six days (JD 277-282, 1996) NSCAT V-pol σ° measurements: (a) projection error standard deviation image prior to azimuth modulation removal, (b) projection standard deviation image after azimuth modulation estimation, (c) magnitude (M_1) of the estimated first-order azimuth modulation harmonic term, (d) magnitude (M_2) of the estimated second-order azimuth modulation harmonic term, (e) phase angle (ϕ_1) of the estimated first-order azimuth modulation harmonic term, and (f) phase angle (ϕ_2) of the estimated second-order azimuth modulation harmonic term. To produce this figure, the 4.45-km pixel resolution has been averaged down to 8.9 km resolution to reduce the image size and match the Escat image pixel resolution.

below), suggesting that the estimated model parameters do not completely explain the azimuth modulation of the data. At least part of the explanation is due to the fact that, as previously noted, the σ° versus azimuth angle modulation exhibits somewhat sharper peaks than the simple second-order Fourier series model is capable of representing. An additional explanation is due to the nonoptimal F model, which does not include the incidence angle dependence of the azimuth modulation. However, as previously noted, sampling limitations prohibit computation of the I model parameters at all locations. We must therefore settle for an approximate result.

Rather than using enhanced resolution images, gridded data can be similarly used to compute the parameters of the I model at lower resolution by accumulating all the measurements over each grid element and using least squares to estimate the I model parameters for the grid element. While not shown here, the direction results are consistent with the higher resolution F model images presented below. Unfortunately, the accuracy and quality of the estimated I model parameters also suffer from the limited azimuth and incidence angle spread of the σ° measurements in some grid elements. The resulting estimate error can be large due to this sampling limitation. Gridded results thus exhibit considerably more noise and as a result have lower subjective quality than the results presented below. The following results include noise filtering in the SIRF algorithm and reduced sensitivity to incidence angle sampling via use of the serial, nonoptimum estimation procedure used for the F model. Noting the general consistency of the I and F model directions, we use the F model approach as a tool to evaluate the azimuth variations in the surface response. Although nonoptimal, this approach can be used for monitoring seasonal variations in the azimuth response.

Fig. 10 presents NSCAT-derived F model images of M_1 , M_2 , ϕ_1 , and ϕ_2 . Though having significantly lower effective resolution, more limited spatial coverage, and reduced accuracy, Escat-derived F model images are presented in Fig. 11. Figs. 10

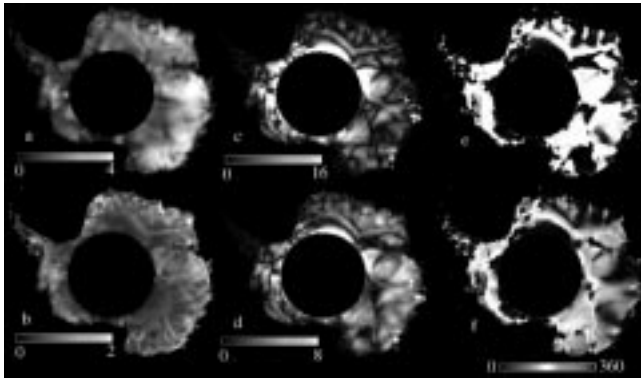


Fig. 11. Escat images from six days (JD 277-282,1996) of σ° measurements: (a) projection standard deviation image prior to azimuth modulation removal, (b) projection standard deviation image after azimuth modulation estimation, (c) magnitude (M_1) of the estimated first-order azimuth modulation harmonic term, (d) magnitude (M_2) of the estimated second-order azimuth modulation harmonic term, (e) phase angle (ϕ_1) of the estimated first-order azimuth modulation harmonic term, and (f) phase angle (ϕ_2) of the estimated second-order azimuth modulation harmonic term. The pixel resolution is 8.9 km.

and 11, together with the \mathcal{A} and \mathcal{B} images shown in Fig. 3, reveal significant variations in the backscatter associated with snow accumulation rates and local variations in topography. Examining the NSCAT images, we note that the regions of smaller surface slopes in central Antarctica exhibit a very high value of \mathcal{A} but that toward the coasts, the value falls off fairly rapidly. The higher \mathcal{B} values in central Antarctica also indicate a flatter σ° versus incidence angle response, suggesting that the scattering is dominated by subsurface volume scattering. In regions dominated by strong katabatic wind flow, the azimuth modulation images generally exhibit large magnitudes coupled with low \mathcal{B} values. This indicates backscattering is dominated by surface roughness in these regions.

The azimuth angle harmonic magnitude images [Fig. 10(c) and (d)] show significant coherent spatial variations in the azimuth modulation of σ° . Interestingly, in the NSCAT images, the crests of the ice divides, separating the major wind and ice sheet drainage basins, display the smallest standard deviations both before and after azimuth modulation removal. This, coupled with the extremely low magnitude values of the first- and second-order harmonic terms, is evidence for virtually no azimuth dependence. Similarly, these correspond with inflection lines in the \mathcal{A} and \mathcal{B} images, implying divides in the accumulation patterns and snow layering as a consequence of the topographically-influenced wind regime. These coupled observations imply lighter winds and lack of directionality in the wind direction (in these locations) with much smoother ice sheet surfaces with negligible aligned roughness and more isotropic backscatter. Such locations, for instance, demonstrate excellent calibration target attributes (provided they exhibit negligible seasonal variability).

We note that the second-order harmonic term [Fig. 10(d)] is generally larger than the first harmonic term [Fig. 10(c)], particularly in the coastal regions of Wilkes Land (90-130E), Princess Elizabeth Land (70-90E), and Terre Adelie (135E). These coastal regions have relatively steep slopes and are known to have stronger focused katabatic winds (funneled

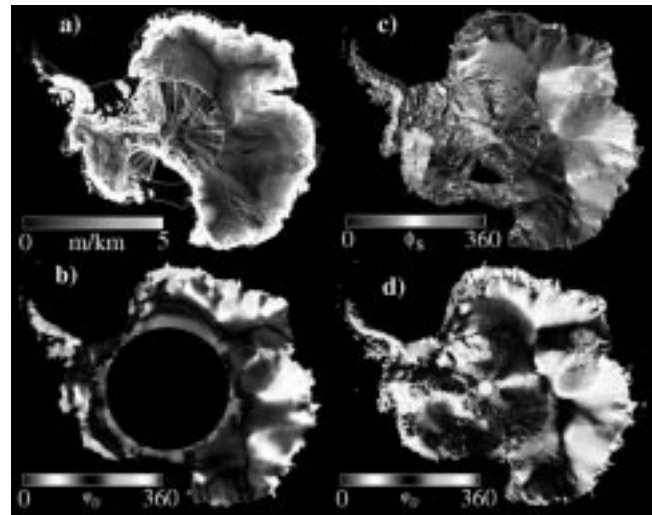


Fig. 12. (a) Magnitude of local slope derived from the topography map. The circle surrounding the pole and cross-hatching are artifacts resulting from the topography map. (b) Escat-derived map of ψ_0 , the direction relative to north of the peak azimuth modulation (F model) from the images in Fig. 11. (c) Direction of the local slope (ϕ_s) derived from the topography map. (d) NSCAT-derived map of ψ_0 , the direction relative to north of the peak azimuth modulation (F model) from the images in Fig. 11.

as they flow outward from the interior regions of Antarctica) coupled with significant microrelief [12], [31]. These regions, not surprisingly, show the largest magnitude modulations in both first and second-order terms. We also note regions of significant second-order azimuth modulation in small areas along the Transantarctic mountains and in western Antarctica as well as in other coastal regions.

The azimuth modulation phase (direction) images [Fig. 10(e), (f)] are most revealing. The inflection lines previously noted in other images are seen to delineate large spatially coherent regions with similar azimuth modulation angle phase terms. This effect is most strongly noted in the second order phase term, though interesting features appear in the first order phase term as well. These phase terms appear to correlate well with the direction of the katabatic wind flow modeled in previous studies [26], [27].

E. Comparison with Topographic Slope

Downslope ice-sheet surface winds are strongly directed by the large scale topography. In this section we compare the NSCAT-derived scattering model parameters with Antarctic topography. The comparison topography map is derived from an Antarctic digital elevation map (DEM) generated from ERS-1 altimeter data by Bamber [2]. Since ERS-1 altimeter coverage is limited to latitudes north of -80° , the TOPO5 database is used to fill in the missing information, with an accompanying loss of accuracy and resolution where used.

The magnitude and direction of the local slope derived from the DEM is shown in the upper panels of Fig. 12. From the topographic high in east-central Antarctica, the slope falls away to the sea in a number of large, well-defined drainage basins. Both large- and medium-scale roughness variations are apparent in the local slope magnitude and direction. Mean large-scale slopes identify flat interior regions of the ice sheet such as Dome Argus (81S 80E) and Dome C (74.5S 123E)

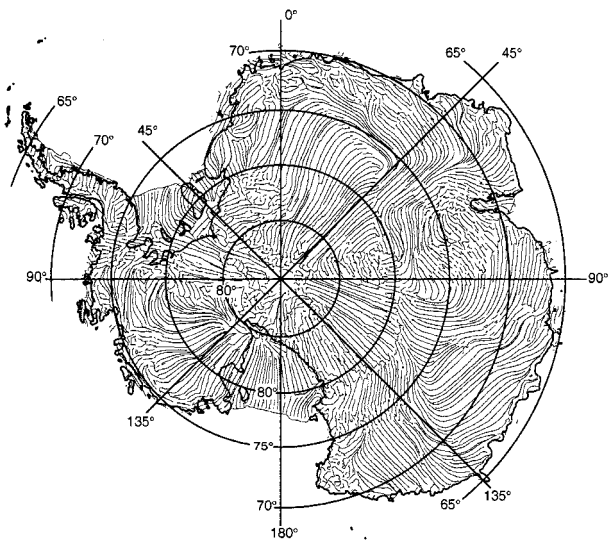


Fig. 13. Streamlines of the direction ψ_0 of the peak azimuth modulation derived from NSCAT data.

and the steep peripheries that end in flat fringes representing the floating ice shelves. Medium-scale texture in the slope map highlights surface undulations resulting from bedrock topography beneath the ice sheet.

The minimum azimuth modulation direction ψ_0 is derived from the estimated F model parameters (in Figs. 10 and 11) for each pixel and is shown for NSCAT and Escat images in Fig. 12. A gray scale was chosen to emphasize the directionality in ψ_0 . Large areas of spatial consistency in the peak direction are observed with correlation to features of the topography. It should be noted that occasionally, the derived peak modulation direction is reversed due to noise, the magnitude of the upwind/downwind ratio, and/or the limited azimuths of the measurements. Thus, occasional pixels with directional reversals relative to nearby pixels are observed. Furthermore, where the slope magnitude is small or the slope direction is highly variable, the surface wind flow is not well defined and a lack of persistence is observed in the wind direction in such regions [26]. This factor presumably prevents formation of coherent structures in the small-scale surface roughness and thus permits larger peak azimuth modulation differences.

Streamlined plots of the model-estimated ψ_0 for NSCAT data is shown in Fig. 13 and for comparison, Escat data in Fig. 14. These plots exhibit a general consistency with the direction of the surface wind flow in previous studies (e.g., [27]). For example, in south Queen Maud Land (0-45° E 75° S) and Terre Adelie (135° E 70° S), the streamlines closely follow the predicted katabatic wind directions. Further, previous measurements made along two Ellsworth Land (90° W 75° S) traverses by [36] suggest sastrugi alignments similar to the directions shown in Fig. 13.

A notable difference is observed between the NSCAT and Escat streamlines on the Hollick-Kenyon Plateau (in West Antarctica 90° W 80° S) where the NSCAT streamlines turn clockwise, and the Escat streamlines continue north. In this region, the NSCAT data shows reduced azimuth modulation, primarily at lower incidence angles, and the minimum is not as well defined as in other

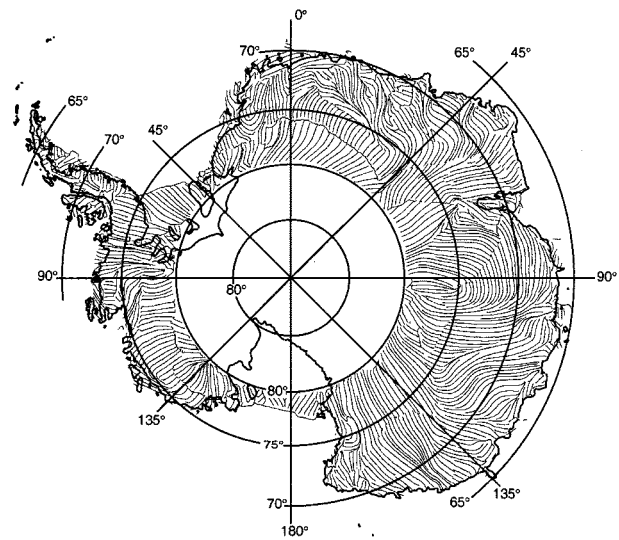


Fig. 14. Streamlines of the direction ψ_0 of the peak azimuth modulation derived from Escat data.

areas. However, the NSCAT data appear to resolve directions that follow the perimeter of the plateau to turn downward onto the Ross ice shelf. The Escat data suggests a small second-order modulation. However, the azimuth sampling is limited, and the resulting F model fit poorly locates the minimum, causing the flowlines to follow the downslope direction rather than turning to the left of the fall line.

V. DISCUSSION

Antarctic anisotropic returns suggest at least two possible mechanisms for azimuth modulation. The first is due to the change in local incidence angle at different azimuth angles because of the slope of large dunes or undulations coupled with large-scale surface topography. This is postulated to cause a first-order modulation. It is possible, however, that the microrelief such as sastrugi on the surface of the larger dunes (but aligned in the wind direction rather than orthogonal to the wind) accounts for second-order harmonics. If this is the case, the resulting returned signal would be a combination of first and second order harmonics caused by the sastrugi being seen at different local incidence angles on the surface of the local topography and km-scale snow dunes. We conjecture that the magnitude of the first harmonic modulation should be greatest in regions where the km-scale and large-scale topography couple to cause the largest effect on the local incidence angle. This appears to be the case in Fig. 10(e) in regions of relatively constant ϕ_1 .

While snow and firn scattering models are well-advanced, the presence of sastrugi has not been modeled. Furthermore, emission models incorporating sastrugi surface roughness are needed to account for the significant modulations to brightness temperatures observed in the coastal regions of East Antarctica. It may be possible to adapt ideas from the two-scale modeling of ocean waves. Scattering models are well-known for ocean waves and recently, Yueh [42] has developed a two-scale emission model. It may be possible to model sastrugi in a similar way. Using such models, microwave data can be used to infer

geophysical parameters of the surface (see [23]). Furthermore, the accuracy of the wind direction estimates could be improved.

While it is possible to draw a number of important conclusions, there are a number of limitations to this study. The primary limitation, one already noted, is the limited range of azimuth angle observations from the sensors. This is a particular problem for passive SSM/I data. As noted, the discrete nature of the azimuth sampling for both NSCAT and Escat arises from the fact that the multiple antennas, at various azimuth angles, are used to make measurements. Errors in the calibration of the individual antennas could introduce and/or modify an apparent azimuth modulation of σ° . Although some potential problems with attitude control have been noted, NSCAT calibration is reported to be within a few tenths of a dB, including interbeam variations [39]. Escat calibration is similarly accurate [22].

We note that the scatterometer is not regarded by the authors as a replacement to anemometers on ice sheets. Previous authors [31], [32] report qualitative relationships between the amplitude of the azimuth modulation and the reported strength of the surface winds, although the precise physical reasoning is uncertain. Similar qualitative relationships might be inferred between the fitted value of M_2 and the wind speed in Fig. 10(d). Mean surface wind speeds are known to range from ~ 2 m/s to over 20 m/s depending on terrain slope, with the latter upper limit common in locations such as Cape Denison (67° S 143° E), and the Terra Nova Bay (75° S 164° E) area, where converging alignments are indicated akin to the convergent modeled katabatic flow streamlines in these regions. Although surface anisotropy connected with the surface wind direction is observed, it is presently difficult to do more than qualitatively sense the magnitude of the wind velocity.

VI. CONCLUSION

For some time, users of radar and radiometer data have made assumptions regarding the transparency or relatively high transmissivity of dry snow surfaces at microwave frequencies. Consequently, air-snow interface roughness has been considered to impart only a limited regional impact on the observed signatures. Many electromagnetic models indicate snow roughness as playing only a minor role in driving variability in the signatures, and some neglect interface roughness by assuming planar layers without any bedding structure. In this paper, we have revealed in greater detail the impact that anisotropic scattering and aligned roughness elements may have on satellite microwave observations. These Antarctic observations clearly demonstrate that models of azimuthal variations in microwave data should account for first- and second-order effects manifested as azimuthal dependencies in SSM/I, Escat, SASS, and NSCAT data. Further studies are required to address the precise mechanisms that drive the observed signatures. While it is clear that the wind causes roughness in the bedding structure and annual layering of accumulated and wind-redistributed snow, it is not clear why alignments ought to be coherent with depth, though coherent internal reflections may play a role. Instruments recording microwave backscatter at different frequencies should be exploited, therefore, to discriminate between physical properties of the snow and firn at varying depths and to address open questions regarding the links between the

firm layer characteristics, wind-induced bedding structures, and the thermodynamic processes linking these physical attributes to the atmospheric conditions on the ice sheet.

Problems exist in fitting simple, single-term models to observations made by each of the instruments due to the limited number of measurements made at discrete azimuth angles in a given region of interest. The outcome is that the slope-dependency of azimuthal modulations is not clearly expressed in any of the previous results documenting efforts to fit simple second-order models to the observations [28], [14]. Our results indicate, in particular, that the local-incidence angle has a clear impact upon the magnitude of the azimuthal modulation. Regions with large slopes and strong expression of meter-scale roughness generate the largest azimuthal modulation in the data. The important additional effect, however, is the lack of symmetry in the azimuthal modulations, which indicates a further effect in areas where km-scale undulations tilt the surface away from the mean slope direction indicated by current digital terrain models. This study effectively demonstrates that both of these important first- and second-order azimuthal terms must be correctly taken into account if the results are to characterize the interdependency between slope and small-scale roughness driving the observed azimuth modulations. Future intercomparisons with RADARSAT SAR data (acquired during the Antarctic Mapping Mission) will help in understanding the morphologic structures influencing the scatterometer data.

NSCAT has proved its unique ability to extract information on polar ice characteristics, and it is clear that scatterometry has an extremely important role to play in the study of the cryosphere [20]. In particular, the combination of scatterometry with SSM/I provides a complementary data set with comparable resolution and contrasting image content. The recent launch of SeaWinds on QuikScat (in May 1999) and the planned launch of SeaWinds on ADEOS-II (in 2000) will extend the existing Ku-band data set obtained by SASS and NSCAT and strengthen our capabilities for characterizing polar snow and ice sheet surface characteristics. With the launch of SeaWinds, Ku-band scatterometer data of unprecedented coverage and quality are being made available. Unlike NSCAT and Escat, SeaWinds is a conically-scanning pencil-beam scatterometer that makes measurements at two incidence angles (42° and 54° over a 1600 km-wide swath) and with a much higher spatial measurement density than NSCAT. As a result, it will be possible to produce images of even higher resolution with improved azimuthal diversity resulting from the conical scan. SeaWinds measurements therefore, hold the promise of long-term observations of the azimuth modulation of Ku-band backscatter to support studies of the long-term variability in surface wind patterns in response to global change.

ACKNOWLEDGMENT

NSCAT data were obtained from the PO.DAAC, Jet Propulsion Laboratory, Pasadena, CA. SSM/I swath data were obtained from the Global Hydrology Resource Center, Global Hydrology and Climate Center, Huntsville, AL. Escat data were analyzed as part of ESA Study AO2.USA119. The authors would like to thank M. Willis, who helped process the SSM/I data, and J. Bamber, who kindly provided the Antarctic ERS-1 altimeter DEM for their use.

REFERENCES

- [1] E. Attema, "The active microwave instrument onboard the ERS-1 satellite," *Proc. IEEE*, vol. 79, pp. 791–799, June 1991.
- [2] J. L. Bamber, "A digital elevation model of the Antarctic ice sheet derived from ERS-1 altimeter data and comparison with terrestrial measurements," *Ann. Glaciol.*, vol. 20, pp. 48–54, 1994.
- [3] A. W. Bingham and M. R. Drinkwater, "Recent changes in the properties of the Antarctic ice sheet," to be published.
- [4] D. J. Cavalieri, J. P. Crawford, M. R. Drinkwater, D. T. Eppler, L. D. Farmer, R. R. Jentz, and E. C. Wackerman, "Aircraft active and passive microwave validation of sea ice concentration from the defense meteorological satellite program special sensor microwave imager," *J. Geophys. Res.*, vol. 96, no. C12, pp. 21 989–22 008, 1991.
- [5] M. R. Drinkwater and D. G. Long, "Seasat, ERS-1/2 and NSCAT scatterometer observed changes on the large ice sheets," in *Proc. Int. Geosci. Remote Sensing Symp. '98*, Seattle, WA, July 6–10, 1998.
- [6] M. R. Drinkwater and V. I. Lytle, "ERS-1 radar and field-observed characteristics of autumn freeze-up in the Weddell Sea," *J. Geophys. Res.*, vol. 102, no. C6, pp. 12 593–12 608, 1997.
- [7] M. R. Drinkwater, D. G. Long, and D. S. Early, "Enhanced resolution ERS-1 scatterometer imaging of southern ocean sea ice," *ESA J.*, vol. 17, no. 4, pp. 307–322, 1993.
- [8] D. S. Early and D. G. Long, "Enhanced resolution imaging from irregular samples," to be published.
- [9] D. S. Early and D. G. Long, "Azimuthal modulation of C-band scatterometer σ^0 over southern ocean sea ice," *IEEE Trans. Geosci. Remote Sensing*, vol. 35, pp. 1201–1209, Sept. 1997.
- [10] M. R. Farrar and E. A. Smith, "Spatial resolution enhancement of terrestrial features using deconvolved SSM/I brightness temperatures," *IEEE Trans. Geosci. Remote Sensing*, vol. 30, pp. 349–355, Mar. 1992.
- [11] Sci. Tech. Inform. Prog., National Aeronautics and Space Administration, Washington, D.C., 1992.
- [12] "ANARE Res. Notes, 64," Antarctic Division, Australia, 1988.
- [13] J. P. Hollinger, J. L. Pierce, and G. A. Poe, "SSM/I instrument evaluation," *IEEE Trans. Geosci. Remote Sensing*, vol. 28, pp. 781–790, Sept. 1990.
- [14] G. Hyland and N. Young, "Wind-induced directional anisotropy of microwave backscatter and its impact on imaging of the Antarctic continental snow cover," in *Proc. Int. Geosci. Remote Sensing Symp. '98*, Seattle, WA, 1998, pp. 1988–1990.
- [15] P. Lecomte, A. Cavanie, and F. Gohin, "Recognition of sea ice zones using ERS-1 scatterometer data," in *Proc. Int. Geosci. Remote Sensing Symp. '93*, 1993, pp. 855–857.
- [16] M. Ledroit, F. Remy, and J. F. Minster, "Observation of the Antarctic ice sheet with the Seasat scatterometer: Relation to katabatic wind intensity and direction," *J. Glaciol.*, vol. 39, no. 132, pp. 385–396, 1993.
- [17] F. Li, G. Neumann, S. Shaffer, and S. L. Durden, "Studies of the location of Azimuth modulation minima for Ku band ocean radar backscatter," *J. Geophys. Res.*, vol. 93, pp. 8229–8238, July 1988.
- [18] D. G. Long and D. Early, "Resolution enhancement of ERS scatterometer data," to be published.
- [19] D. G. Long and D. Daum, "Spatial resolution enhancement of SSM/I data," *IEEE Trans. Geosci. Remote Sensing*, vol. 36, pp. 407–417, Mar. 1997.
- [20] D. G. Long and M. R. Drinkwater, "Cryosphere applications of NSCAT data," *IEEE Trans. Geosci. Remote Sensing*, vol. 37, pp. 1671–1684, May, 1998.
- [21] D. G. Long, "NSCAT views land and ice," in *Proc. Int. Geoscience and Remote Sensing Symp.*, Seattle, WA, July 6–10, 1998, pp. 1973–1975.
- [22] D. G. Long and G. B. Skouson, "Calibration of spaceborne scatterometers using tropical rainforests," *IEEE Trans. Geosci. Remote Sensing*, vol. 34, pp. 413–424, Mar. 1996.
- [23] D. G. Long and M. Drinkwater, "Greenland ice-sheet surface properties observed by the Seasat-A scatterometer at enhanced resolution," *J. Glaciol.*, vol. 40, no. 135, pp. 213–230, 1994.
- [24] D. G. Long, P. Hardin, and P. Whiting, "Resolution enhancement of spaceborne scatterometer data," *IEEE Trans. Geosci. Remote Sensing*, vol. 31, pp. 700–715, May 1993.
- [25] F. M. Naderi, M. H. Freilich, and D. G. Long, "Spaceborne radar measurement of wind velocity over the ocean—an overview of the NSCAT scatterometer system," *Proc. IEEE*, vol. 79, pp. 850–866, June 1991.
- [26] T. R. Parish, "Surface airflow over east Antarctica," *Mon. Weather Rev.*, vol. 110, pp. 84–90, 1982.
- [27] T. R. Parish and D. H. Bromwich, "The surface windfield over the Antarctic ice sheet," *Nature*, vol. 328, pp. 51–54, 1987.
- [28] W. Rack, "Streuverhalten und morphologie der Antarktischen schneedecke aus scatterometer-messungen von ERS-1," Ph.D. dissertation, Univ. Innsbruck, Innsbruck, Austria, 1995.
- [29] Q. P. Redmund and D. G. Long, "Polar sea ice extent mapping using Ku-band scatterometer data," *J. Geophys. Res.*, 1998.
- [30] ———, "Optimization of SIRF for NSCAT," Tech. Rep. 97-003, Microw. Earth Remote Sensing Lab., Brigham Young Univ., Provo, UT, 1997.
- [31] F. Remy, M. Ledroit, and J. F. Minster, "Katabatic wind intensity and direction over Antarctica derived from scatterometer data," *Geophys. Res. Lett.*, vol. 19, pp. 1021–1024, 1992.
- [32] F. Remy and J. F. Minster, "A comparison between active and passive microwave measurements of the Antarctic ice sheet and their association with the surface katabatic winds," *J. Glaciol.*, vol. 37, no. 125, pp. 3–10, 1991.
- [33] W. D. Robinson, C. Kummerow, and W. S. Olson, "A technique for enhancing and matching the resolution of microwave measurements from the SSM/I instrument," *IEEE Trans. Geosci. Remote Sensing*, vol. 30, pp. 419–429, May 1992.
- [34] H. Rott, "Synthetic aperture radar capabilities for glacier monitoring demonstrated with Seasat SAR data," *Z. Gletscher. Glazial.*, vol. 16, pp. 255–266, 1980.
- [35] R. Sethmann, B. A. Burns, and G. C. Heygster, "Spatial resolution improvement of SSM/I data with image restoration techniques," *IEEE Trans. Geosci. Remote Sensing*, vol. 32, pp. 1144–1151, Nov. 1994.
- [36] H. Shimizu, "Glaciological studies in west Antarctica, 1960–62," *Antarctic Snow and Ice Studies*, vol. 2, pp. 37–64, 1964.
- [37] A. Stogryn, "Estimate of brightness temperatures from scanning radiometer data," *IEEE Trans. Antennas Propagat.*, vol. AP-26, pp. 720–726, Sept. 1978.
- [38] R. H. Thomas, R. A. Bindschadler, R. L. Cameron, F. D. Carsey, B. Holt, T. J. Hughes, C. W. M. Swithinbank, I. M. Whillans, and H. J. Zwally, "Satellite remote sensing for ice sheet research," Tech. Memo., National Aeronautics and Space Administration, Washington, DC, vol. 86 233, 1985.
- [39] W. Tsai, J. E. Graf, C. Winn, J. N. Huddleston, R. S. Dunbar, M. H. Freilich, F. J. Wentz, D. G. Long, and W. L. Jones, "Post-launch sensor verification and calibration of the the NASA scatterometer," *IEEE Trans. Geosci. Remote Sensing*, vol. 37, pp. 1517–1542, May 1999.
- [40] F. J. Wentz, "Measurement of oceanic wind vector using satellite microwave radiometers," *IEEE Trans. Geosci. Remote Sensing*, vol. 30, pp. 960–972, Sept. 1992.
- [41] V. R. Wismann and K. Boehnke, "Monitoring snow properties on greenland with ERS scatterometer and SAR," in *3rd ERS Symp.*, Florence, Italy, Mar. 1997.
- [42] S. H. Yueh, R. Kwok, S. Lou, and W. Tsai, "Sea ice identification using dual-polarized Ku-band scatterometer data," *IEEE Trans. Geosci. Remote Sensing*, vol. 35, pp. 560–569, May 1997.
- [43] H. J. Zwally, A. C. Brenner, J. A. Major, R. A. Bindschadler, and J. G. Marsh, "Growth of the greenland ice sheet," *Science*, vol. 246, pp. 1587–1591, 1989.
- [44] H. J. Zwally and S. Fiegles, "Extent and duration of Antarctic surface melt," *J. Glaciol.*, vol. 18, pp. 195–215, 1994.



David G. Long (M'89–SM'98) received the Ph.D. degree in electrical engineering from the University of Southern California, Los Angeles, in 1989.

From 1983 to 1990, he worked for the National Aeronautics and Space Administration's Jet Propulsion Laboratory (JPL), California Institute of Technology, Pasadena, where he developed advanced radar remote sensing systems. While at JPL, he was the Senior Project Engineer on the NASA Scatterometer (NSCAT) Project, which was flown aboard the Japanese Advanced Earth Observing System (ADEOS) from 1996 to 1997. He is currently a Professor in the Electrical and Computer Engineering Department, Brigham Young University, Provo, UT, where he teaches upper division and graduate courses in communications, microwave remote sensing, radar, and signal processing. He is the Principle Investigator on several NASA-sponsored interdisciplinary research projects in remote sensing, including innovative radar systems, spaceborne scatterometry of the ocean and land, and modeling of atmospheric dynamics. He is a Member of the NSCAT and SeaWinds Science Working Teams. He has numerous publications in signal processing and radar scatterometry. His research interests include microwave remote sensing, radar theory, space-based sensing, estimation theory, computer graphics, signal processing, and mesoscale atmospheric dynamics.



Mark R. Drinkwater (M'88) was born in Oldham, U.K., in 1963. He received the B.Sc. degree (with honors) from Durham University, Durham, U.K., in 1984, specializing in remote sensing in glaciology, and a Council of Europe Diploma in remote sensing in engineering from the University of Dundee, Dundee, U.K., in 1984. For his doctorate research, he studied at Emmanuel College, Cambridge, U.K., and the Scott Polar Research Institute, University of Cambridge, where he received the Ph.D. degree in geophysics in 1988.

From 1987 to 1988, he was a Consulting Research Scientist with Polar Oceans Associates, Cambridge, a Division of Science Applications International Corporation. In 1988, he was awarded a National Research Council Resident Research Associateship, and until 1990, he was with the Polar Oceanography Group, Jet Propulsion Laboratory (JPL), California Institute of Technology, Pasadena. From 1990 to 2000, he was a Research Scientist with the Ocean Sciences Research Element, JPL, working on several international projects with NASA, ESA, CSA, and NASDA. Since May 2000, he has been with the European Space Agency (ESA), where he is Head of the Oceans/Sea-Ice Unit of the Earth Sciences Division, European Space Research and Technology Centre (ESTEC), Noordwijk, The Netherlands. He has published over 40 refereed journal articles, several book chapters, and over 40 conference papers. His professional interests involve microwave remote sensing of the polar oceans and terrestrial ice sheets. Recent focuses include geophysical data extraction, inverse electromagnetic scattering, and coupling EM and thermodynamic models with massively parallel general circulation models for large-scale estimates of surface fluxes of heat and salt in the polar oceans.

Dr. Drinkwater is a member of the International Glaciological Society, the IEEE Geoscience and Remote Sensing Society, and was recently an Associate Editor of the American Geophysical Union's *Journal of Geophysical Research, Oceans*.